Laser micro-machining of hydrophobic-hydrophilic patterns for fluid driven self-alignment in micro-assembly

Gert-willem RÖMER[*1], Mark JORRITSMA[*1], Daniel ARNALDO DEL CERRO[*1],
Bo CHANG[*2], Ville LIIMATAINEN[*2], Quan ZHOU[*2] and Bert HUIS IN 'T VELD[*1,3]

[*1] *University of Twente, Faculty of Engineering Technology, Chair of Applied Laser Technology, Drienerlolaan 5, 7522 NB, Enschede, The Netherlands*
E-mail: g.r.b.e.romer@utwente.nl
[*2] *Aalto University, Electrical Engineering, Department of Automation and Systems Technology, 00076 Aalto, Finland*
[*3] *TNO Science & Industry, Department Materials Technology, De Rondom 1, 5600 HE, Eindhoven, The Netherlands*

Fluid driven self-alignment is a low cost alternative to fast but relatively inaccurate robotic pick-and-place assembly of micro-fabricated components. This fluidic self-alignment technique relies on a hydrophobic-hydrophilic pattern on the surface of the receiving substrate, which confines a fluid to a receptor site. When a micro-component is dropped on the fluid capillary forces drive the assembly process, resulting in accurate positioning of the part relative to the site. This paper demonstrates the advantages of the use of an ultra short pulse laser, with pulse durations in ps regime, to create receptor sites (ranging from $110\times110\mu m^2$ up to $5\times5mm^2$) from which liquid spreading is stopped by a sharp geometrical modification around the site. It was found, by video based optical contact angle measurement, that the volume of water that is pinned on the receptor site increases with increasing angle of the edges of the receptor site. In addition, it was found, by using a robotic microassembly system, that the success rates of self-alignment of $110\times110\mu m^2$ parts, as well as $200\times200\mu m^2$ parts, on the receptor sites is 100% if angle of the edges of the receptor site are sharp, and the height of the receptor site is well over the initial surface roughness of the substrate.

Keywords: Laser, Ultra short laser pulse, hydropobic/hydrophilic patterning, self-alignment

1. Introduction

Ultra short pulse lasers (USPL), with pulse durations in ps regime and smaller, have proven to be versatile tools for introducing functional features in surfaces at a micrometric and even at a sub-wavelength scale [1,2]. Being able to control the surface topography at this level provides, for example, a method to change the wetting behaviour (hydrophobicity and hydrophilicity) of a great number of materials. As such, micromachining with USPLs allows for fast, flexible and accurate control of the surface topography, hence of the wetting properties of surfaces. This paper studies the use of a ps laser source for the fabrication of hydrophobic-hydrophilic patterns on a substrate to allow for fluid driven self-alignment.

1.1 Fluid driven self-aligment

Fluid driven self-alignment is a low cost alternative to fast, but relatively inaccurate robotic pick-and-place assembly of micro-fabricated components [3,4]. For example in 3D integration of functional components, such as IC's, into highly integrated micro- and nano-systems [4], see Figure 1. The fluidic self-alignment technique relies on a hydrophobic-hydrophilic pattern on the surface of the receiving substrate, which confines the fluid to a receptor site (Figure 1b). When a micro-component, with dimensions in the order of $100\times100\ \mu m^2$, is "dropped" on the fluid (Figure 1c and d), capillary forces drive the alignment of the part to the receptor site (Figure 1e) [5]. When the shape, as well as the relative wetting properties of the receptor site, as well as of the part, are optimized, this self-alignment

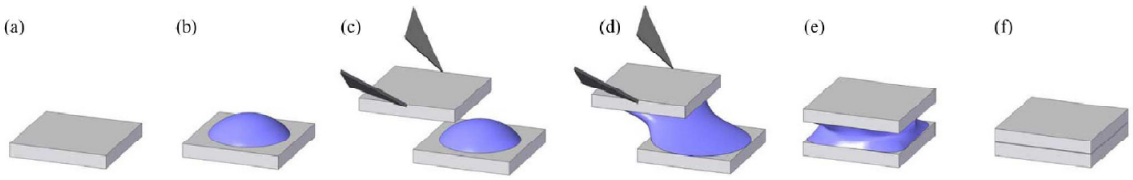

Fig. 1 Fluid driven self-alignment: (a) Receptor site, (b) a droplet of a liquid is dispensed on the receptor site, (c) a gripper approaches the site with a part, (d) the part contacts with the droplet, (e) the gripper releases the part and the capillary force aligns the parts, (f) the liquid between the two parts evaporates, which leaves the two parts aligned [4].

technique allows for accurate positioning (about ±2 μm) of the part to the receptor site. Orientation accuracies of the part relative to the receptor site of typically ±0.5° have been reported [4,5]. Moreover, it was shown, that capillary forces can overcome initial positioning errors (Figure 1d) of up to 180μm in the case of a part of 300×300μm^2 [6,7].

1.2 Three methods to functionalize the substrate

In order to pin liquid to the receptor site, the surface of the substrate needs be functionalized. That is, an area with a boundary, showing a high contrast in wetting properties across it, needs to be created. The change in wetting properties across this boundary will limit the advancing of the liquid, and, as such, prevents the spreading of the liquid out of the receptor area. In general, two factors determine the wetting properties of a surface [8], that is, its:

i. chemical composition,
ii. topography, which can be subdivided into factors related to the geometrical features on the surface:
    a. roughness or texture, which is a factor defined for areas of the surface, and
    b. obstacles or edges which is a factor defined for "lines" on the surface.

The first factor (*i*), is based on creating a hydrophobic/hydrophilic pattern by locally changing the substrate chemical composition. A liquid will preferably spread on areas with a high surface energy, e.g. materials with an ionic, covalent or metal binding [9], while areas with a low surface energy, like plastics or molecular crystals, are usually hardly wetted [9]. The contact angle that a liquid drop forms over a surface is a measure of the tendency of the liquid to wet the solid [10], and it is determined by the balance of the solid-vapour, solid-liquid and liquid-vapour surface tensions at the interface, see Figure 2.

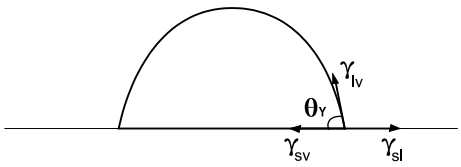

Fig. 2 Definition of contact angle.

For a flat and homogenous surface, this angle is given by the Young's equation [11]:

$$\cos\theta_Y = \frac{\gamma_{SV} - \gamma_{SL}}{\gamma_{LV}}, \qquad (1)$$

where θ_Y is Young's equilibrium contact angle, and γ_{SV}, γ_{SL}, and γ_{LV} are respectively the solid-liquid, solid-vapour and liquid-vapour interfacial surface tensions.

When the liquid phase is water, a solid is commonly called to be hydrophilic if θ_Y is below 90°, and hydrophobic if θ_Y is above this value [9]. Applying a top coating with opposite wetting properties to those of the substrate will generate the desired phobic/philic pattern, see Figure 4a and 4b.

The second factor (*ii*a) is based on limiting the spreading of a liquid by adjusting the substrate roughness. It is well known that roughness amplifies the wetting properties of a substrate [12, 13, 9, 1]. A liquid spreads on a rough surface until it reaches an apparent contact angle that can be calculated by two models, developed separately by Wenzel [14] and Cassie and Baxter [15]. According to the Wenzel model, the liquid homogeneously wets the rough substrate (see Figure 4c, right) to form an apparent contact angle θ_W that is given by

$$\cos\theta_W = r \cdot \cos\theta_Y, \qquad (2)$$

where θ_W is the apparent contact angle that a liquid forms on the rough surface, r [-] is a measure of the solid roughness, defined here as the ratio between its surface and projected areas. And, as mentioned above θ_Y is the Young's equilibrium contact angle of the smooth surface As r>1, increasing the roughness of a surface with a θ_Y above 90° will enhance the liquid repellant properties of the substrate. When θ_Y < 90°, the spreading of the liquid will be enhanced. The Cassie-Baxter model assumes the existence of a mixed wetting state, where air pockets remain trapped below the water drop, in a way that only the tops of the surface features are in contact with the liquid. A liquid under this wetting state will roll of the area with a small tilting [16]. The apparent contact angle θ_{CB} for this state is given by

$$\cos\theta_{CB} = f\left(\cos\theta_Y + 1\right) - 1, \qquad (3)$$

where θ_{CB} is the apparent contact angle that a liquid forms on the rough surface, f is the fraction of the solid area that it is in contact with the liquid. Again, θ_Y is Young's contact angle of the smooth surface.

The third factor (*ii*b) consists of preventing the liquid spreading by creating a sharp geometrical modification around the target area that is able to stop the advancing of the liquid-solid-vapour interface. When a liquid front reaches an edge, a local contact angle θ [deg] will be formed according to the so-called Gibbs condition [17]

$$\theta_Y < \theta < (180 - \alpha) + \theta_Y, \qquad (4)$$

where α [deg] is the edge angle, see Figure 3. Sharper edges, thus with smaller α values, have proven to be able to confine larger amounts of liquid within the target area, before the liquid front is able to cross the modified perimeter [17,18].

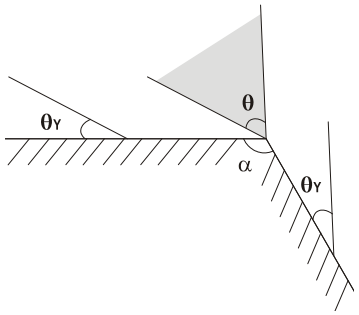

Fig. 3 Definition of solid angle α [17,18].

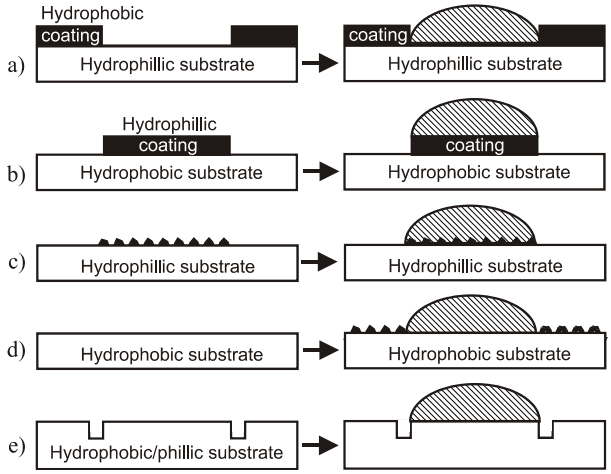

Fig. 4 Alternatives to create hydrophobic/hydrophilic patterns on a smooth surface which is either hydrophobic or hydrophilic by nature.

In the view of the above physical phenomena governing wetting, three alternatives for creating hydrophobic/hydrophilic patterns, created by laser micromachining, for liquid driven self-alignment could be considered, see Figure 4:

1. If the surface is hydrophilic, the chemical composition of the surface can be modified by applying a hydrophobic coating on top. Subsequently, this coating can be selectively removed by laser machining (Figure 4a), to create a receptor site which is hydrophillic. Hydrophilic sites on a hydrophobic substrate can be created by applying a hydrophilic coating at the desired positions (Figure 4b).
2. Increasing the roughness of the receptor site by use of the laser, see Figures 4c and 4d. If the substrate is hydrophobic, the increased roughness yields higher apparent contact angles, and therefore limits the liquid spreading. An alternative way to keep areas is achieving the Cassie-Baxter state for all the areas that shall remain non-wetted (dry). When the substrate is hydrophilic, a proper selection of the roughness allows a given liquid volume to spread only over the laser processed area (Figure 4c) [1,19,20].
3. Creating edges/obstacles by material removal from a laser track, see Figure 2f. An edge (or trench) around the receptor site can be created by removing material from the tracks of a laser path that follows the perimeter of the receptor site. The edges of the tracks will provide a location for the pining of the liquid-solid-vapour interface, and sharp edges can be accurately machined by a proper selection of the laser processing parameters. Note that this approach will work for hydrophobic as well as hydrophilic substrates.

In this paper a so-called leadframe, which is used in the semiconductor industry as a base for die bonding and packaging, will be studied as a substrate, see section 3.1. As the surface composition of the top-layer of the leadframe is typically hydrophilic, most of the liquids that can be considered for the self-alignment process will tend to spread out of the receptor site. There is therefore a need to confine the liquid into the receptor site. As discussed above, this can be achieved by processing areas or by creating a sharp edge around the receptor site. Among the available alternatives, the creation of the sharp edges will be selected as the topic of study for this paper. This is because processing lines with a laser is in general much a faster process than modifying the whole receptor site. In addition, the trapping of the liquid can be achieved in a single processing step if the proper geometry of the edge is achieved. Moreover, there is no need to chemically functionalize the substrate, in that case.

2. Scope of this paper

The next section describes the material (substrate), experimental setup. Section 4 describes the experimental results. That is, first the ablation threshold under ps-laser radiation of the lead frame (substrate) was determined. This threshold provided input for determination of laser processing conditions to create trenches around square receptor sites. Trenches were produced around receptor sites of four sizes: about 5×5mm^2, about 110×110µm^2, about 200×200µm^2 and about 210×210µm^2. The 5×5 mm^2 sites allowed initial analysis of the wetting and liquid confinement properties using standard video based optical contact angle measuring equipment, see section 3.3. Whereas, a microassembly system was used to carry out self-alignment tests on receptor sites of 110×110 µm^2 and 200×200µm^2, see section 3.4. Finally, the receptor sites of 210×210µm^2 were used to test their liquid confinement ability. Trenches of several depths, widths and shape were created to study the dependence of the geometry of the receptor site and trenches on the liquid confinement capability, as well as on the self-alignment capability of the site. Finally, sections 5 and 6 contain conclusions and an outlook to future work.

3. Material and experimental set-up

3.1 Material

The substrate under consideration is a leadframe, which is composed of a copper foil (bulk), with a standard roughened PrePlated leadframe Finish (PPF), see Figure 5. Details on the motivation of this composition of the lead frame fall outside the scope of this paper. A protective foil, which covers the leadframe, was removed just before laser machining.

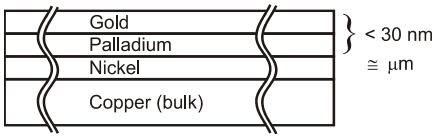

Fig. 5 Cross section of the material applied as the substrate (lead frame) with NiPaAu finish. Note the thickness of the layers are not to scale in the graph.

3.2 Laser set-up

An Yb:YAG laser source, type TRUMICRO 5050 of TRUMPF GMBH, Germany, with a central wavelength of 1030 nm (IR) was used for generation of the laser pulses. But for the experiments, a Third Harmonic Generation (THG) unit was applied to convert the central wavelength to 343nm (UV), as the absorption of laser energy of the substrate at this wavelength is higher than at IR. Moreover, the UV wavelength, in contrast to the IR wavelength, al-

lows for focusing the laser beam into a smaller diameter (see section 4.1), which, in turn, allows machining of smaller features. The maximum average power available in UV is about 15 W at (a maximum) pulse frequency of 400 kHz. The beam shows a nearly Gaussian power density profile, see Figure 6. The pulse duration was constant at 6.7ps for all experiments. The radiation was linearly polarized (horizontally).

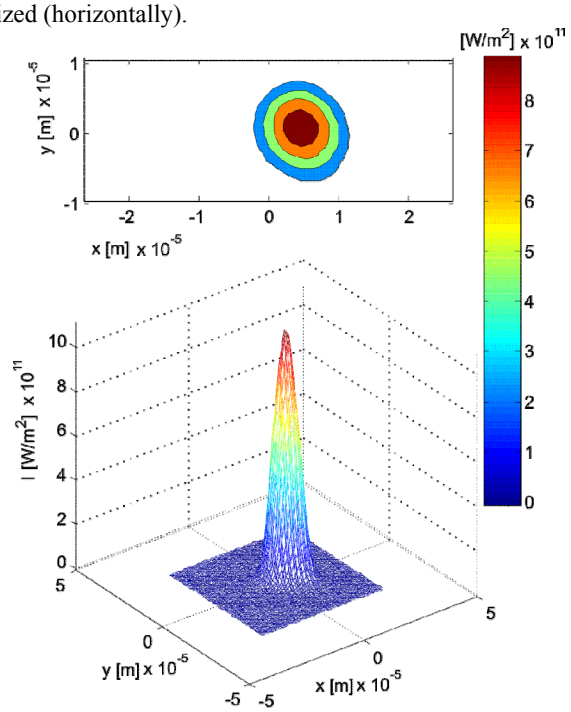

Fig. 6 Power density distribution, in focus, of the applied laser beam at 200kHz and 100mW, measured using a MICROSPOTMONITOR of PRIMES GMBH, of Pfungstadt, Germany, and analyzed using the MATLAB Laser Toolbox [21].

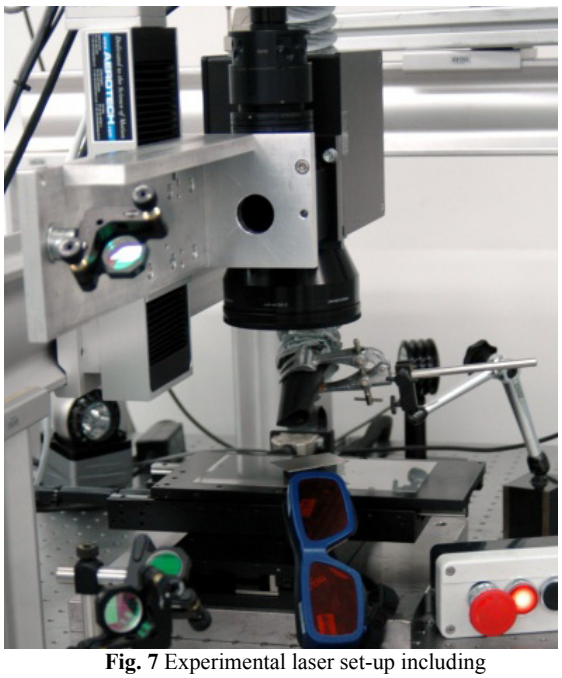

Fig. 7 Experimental laser set-up including the galvoscanner and telecentric *f*θ-lens.

Manipulation of the beam over the samples was accomplished by a two mirror galvo scanner system, see Figure 7, type INTELLISCAN14 of SCANLAB GMBH, of Puchheim, Germany. A telecentric 100 mm *f*θ-lens, type RONAR of LINOS GMBH, of Göttingen, Germany, focused the beam. The substrate was irradiated at normal incidence at environmental conditions.

After laser machining, the substrate was cleaned in an ultrasonic bath with acetone for 5 minutes, and subsequently with IPA for 5 minutes.

3.3 Analysis tools

The surface topography of the machined surfaces were analyzed by a Confocal Laser Scanning Microscope (CLSM), type VK-9700, of KEYENCE, Osaka, Japan and a Scanning Electron Microscope (SEM), type JCM NEOSCOPE 5000 of JEOL LTD., Tokyo, Japan. The wetting properties of the samples, at room temperature, were determined by a video based optical contact angle measuring device, the OCA15plus of DATAPHYSICS INSTRUMENTS GMBH of Filderstadt, Germany, using distilled deionized water droplets of 4 microliters.

3.4 Set-up for self-alignment tests

A microassembly system was used to carry out self-alignment tests [4]. The system includes a robotic microgripper, two microscopes, three motorized stages and a droplet dispenser, see Figure 8.

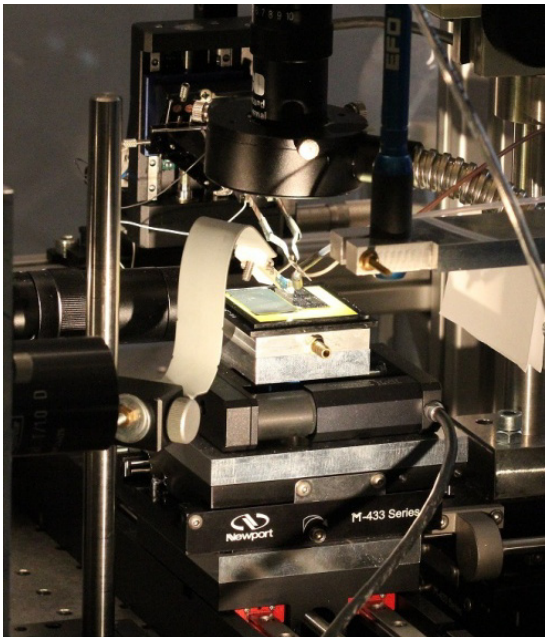

Fig. 8 The microassembly system used to carry out self-alignment tests [4].

The microgripper is custom built, driven by two piezoelectric benders. The motorized stages provide movement in *x*-,*y*- and *z*-directions. The *z*-axis stage (type M-122.2DD of PHYSIK INSTRUMENTE, Karlsruhe, Germany) moves the microgripper vertically, while the *x*-axis stage (type M-122.2DD of PHYSIK INSTRUMENTE) and y-axis stage (type M-404.8PD of PHYSIK INSTRUMENTE) move the test patterns (leadframe) horizontally. The droplet dispenser (type

PicPIP of GESIM, Grosserkmannsdorf, Germany) is non-contact type, actuated by a piezoelectric diaphragm. It can dispense droplets in a distance of a few millimeters with a resolution of tens of pico liters depending on the control parameters.

The self-alignment process was imaged from a top view microscope (type VZM1000i of EDMUND, Nether Poppleton, UK) and a side view microscope (type VZM1000i, EDMUND). A high-speed CMOS video camera (type IPX-VGA210-G of IMPERX of Boca Raton, USA) was attached to the top microscope and a CCD video camera (type scA1600-14gc of BASLER, Ahrensburg, Germany) has been attached to the side view microscope.

4. Results and discussions

Measurements, using the CLSM, showed that the surface roughness of the unmachined substrate was $R_a \approx 1.5\mu m$. Note that this is much larger than the thickness of the palladium and gold layers, and of the same order of magnitude as the nickel layer. The roughness was found to result from a polishing step during the production of the leadframe.

4.1 Ablation threshold

Next, the ablation threshold, or more specifically the fluence threshold, above which the substrate under laser radiation, will be ablated, was determined using a method usually referred to as the *D^2-method* [22-24]. In accordance with this approach, the material was exposed to single laser pulses, at several pulse energy levels. The diameter D [m] of each ablated crater was determined by CLSM. Figure 9 shows this squared diameter D^2, as function of the pulse energy. In accordance with the D^2-method, the beam diameter was determined from the slope of this curve, to equal 15.6 μm. The determination of the ablation threshold relies on the linear relation between squared diameter D^2 and the logarithm of the applied pulse fluences. The ablation threshold follows from the extrapolation of the curve in Figure 9 to the lower horizontal axis. The ablation threshold was found to be 0.11 J/cm^2, which corresponds to a pulse energy of 0.10 μJ at the given spot diameter.

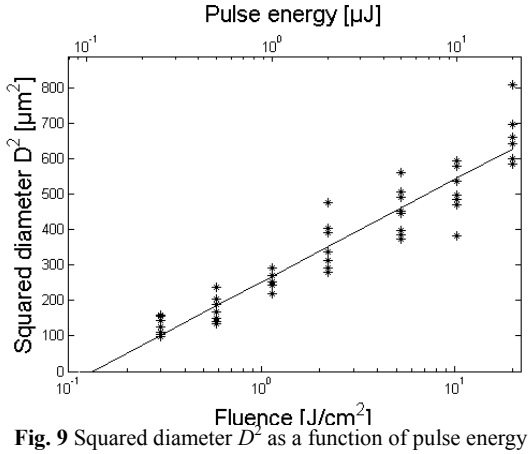

Fig. 9 Squared diameter D^2 as a function of pulse energy (upper horizontal axis) and as function of fluence (bottom axis).

Bonse et al. showed that the ablation threshold reduces with increasing number of pulses applied to the substrate [23]. This incubation effect, which can be attributed to the accumulation of (absorbed) energy, is ignored here. That is, because the sole aim of the determination of the threshold was to obtain initial processing conditions to create trenches.

4.2 Processing conditions for single laser tracks

Next, laser machining conditions were determined to create trenches with targeted depths of 0.5 μm, 1.0 μm, 2.0 μm and 5.0 μm. To that end first single lines were machined with the laser. To check whether the laser radiation of a pulse intervenes with the plasma generated by ablation induced by a previous pulse (plasma shielding), as well as to avoid any temperature build up in the substrate due to accumulation of heat, the pulse repetition frequency was initially fixed to 50 kHz. At this pulse repetition frequency the pulse energy E_p [J] and number of overscans N were varied between, respectively E_p= 0.05μJ and 0.25μJ and N=10 and 1000. The pulse to pulse distance between subsequent pulses was fixed to 0.5 μm. The low laser pulse energies applied here, were chosen to ensure that only the upper part of the Gaussian power density profile was above the ablation threshold. Next, the pulse repetition frequency was set to 400kHz and pulse energy and number of overscans were varied between, respectively E_p= 0.10μJ and 0.15μJ and N=10 and 1000. The pulse to pulse distance was fixed to 0.5μm again, in these experiments. No significant differences were found between the results of machining at 50kHz to machining at 400kHz. Therefore a pulse repetition frequency of 400 kHz can be used without plasma shielding or accumulation of heat in the substrate, while having the advantage of a faster processing speed.

Finally, at 400 kHz the pulse to pulse distance was increased to 1.0μm to investigate the influence of this distance on the ablated geometry. To that end, the beam velocity v was varied between 200 mm/s and 400 mm/s, to obtain a pulse to pulse distance of either 0.5μm or 1.0μm. This implies a pulse overlap OL [%] of 97% and 94% respectively, when the overlap is defined as

$$OL = 1 - \frac{v}{d \cdot f_p} \times 100\% \qquad (5)$$

where v [m/s] denotes the velocity of the laser beam relative to the substrate, d [m] the diameter of the laser beam on the surface of the substrate (here the focus diameter of 15.6 μm) and f_p [Hz] the pulse repetition frequency of the laser source.

Figure 10 shows a SEM image and CLSM measurements of two typical single “laser tracks” or ablated “lines”. Evident in Figure 10a and 10b are horizontal grooves (or scratches) caused by the horizontal polishing of the lead frame leading to the aforementioned surface roughness. These grooves have a significant impact on the edge quality of the ablated lines, see Figure 10a and 10b. From the SEM image (Figure 10a) is can be observed that some ablated material was deposited on the edges of the tracks. Figure 10b and 10c show an isometric representation of CLSM measurements, and a cross section respectively, of the same lines as depicted in Figure 10a. Geometrical parameters of the tracks, defined in Figure 11, were determined from the CLSM cross sections.

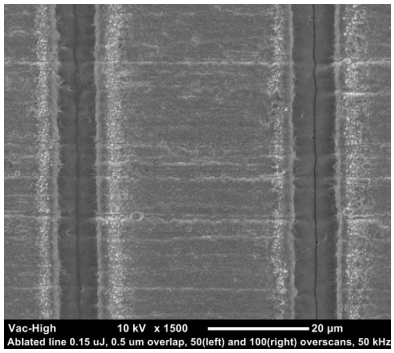

(a) SEM image,
10kV × 1500, Vac-High. Scale bar 20µm

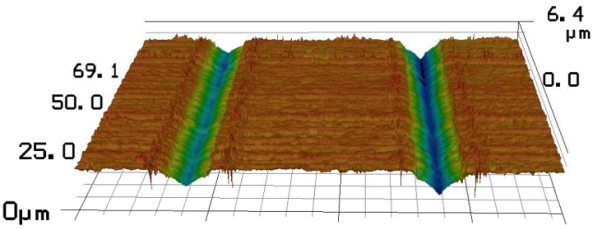

(b) CLSM isometric

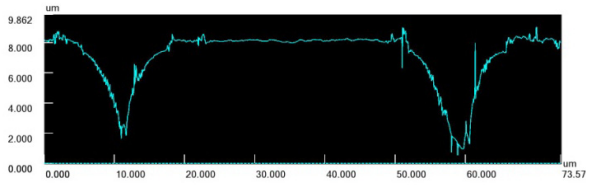

(c) CLSM cross section.

Fig.10 SEM and CLSM images of two laser tracks/lines. E_p=0.15 µJ, N=50 (left), N=100 (right).

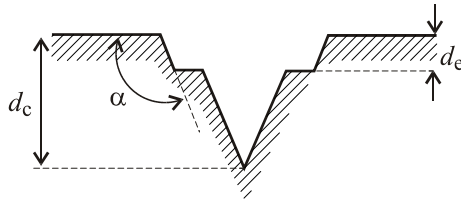

Fig. 11 Definition of geometrical dimensions: track edge depth d_e, track edge angle α and track center depth d_c.

The cross section clearly shows a sharp change in ablated height at the edges of the ablated line, defined here as the track edge depth d_e [µm]. It is assumed that this sharp change in height is caused by the removal/ablation of the PPF layer (Figure 5). Closer to the center of the track, the tracks deepen with a certain curvature to the track center depth d_c [µm].

Figures 12 and 13 show the track edge depth d_e, as a function of pulse energy E_p and number of overscans N, at pulse repetition frequencies of 50 kHz and 400 kHz respectively. As can be observed from these figures, the ablated track edge depth d_e has a maximum of about 1.5 to 2.5µm. This implies that the PPF layer was completely removed and for some processing conditions some of the copper below is removed as well.

Figure 14 and 15 show the of the track center depth d_c, measured by CLSM, as a function of pulse energy and number of overscans at pulse repetition frequencies of 50 kHz and 400 kHz respectively.

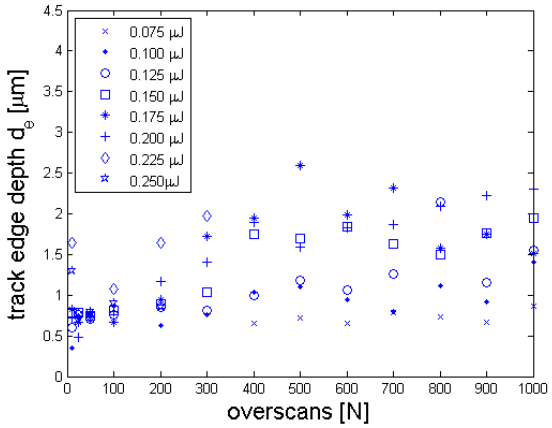

Fig. 12 Measured ablated track edge depth, as a function of pulse energy, overlap and number of overscans at 50 kHz.

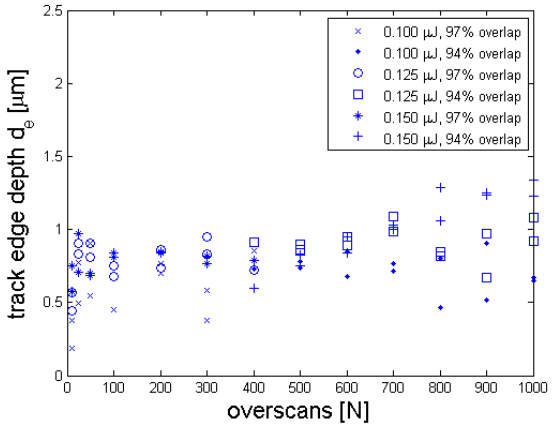

Fig. 13 Measured ablated track edge depth as a function of pulse energy, overlap and number of overscans at 400 kHz.

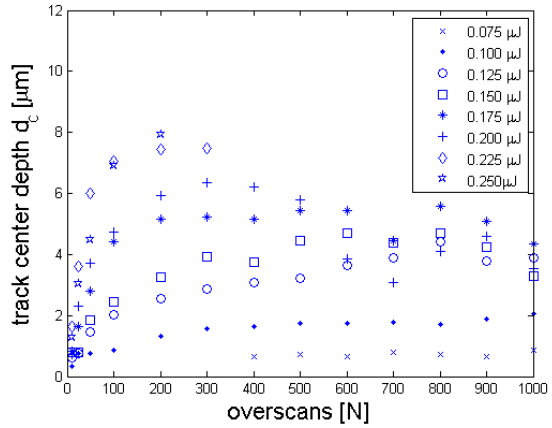

Fig. 14 Measured ablated track center depth, as a function of pulse energy and number of overscans at 50 kHz.

Both Figure 14 and 15 show that, in contrary to the edges of the track, the depth d_c of the center of the tracks increase with increased pulse energy and overscans.

As the liquid confinement capability of a receptor site depends on the geometrical angle of the edges of the site (see section 1.2), the edge angle α [deg], as defined in Figure 11, of the laser generated tracks were measured by CLSM. Figure 16 and 17 show the of the edge angle α as

a function of pulse energy, overlap and number of overscans at pulse repetition frequencies of 50kHz and 400kHz respectively.

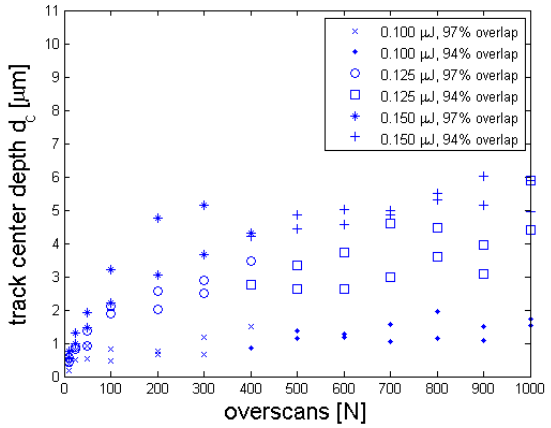

Fig. 15 Measured ablated track center depth, as a function of pulse energy and number of overscans at 400 kHz.

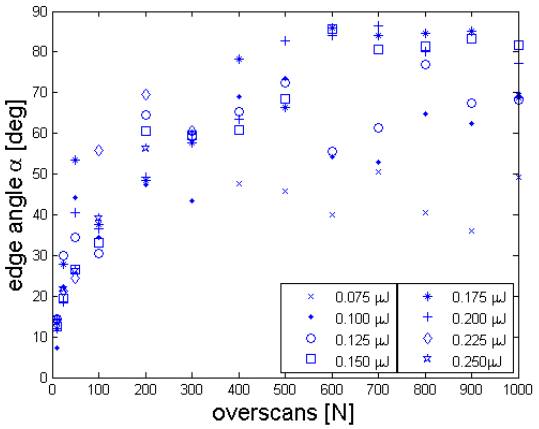

Fig. 16 Measured edge angle as a function of pulse energy and number of overscans at 50 kHz.

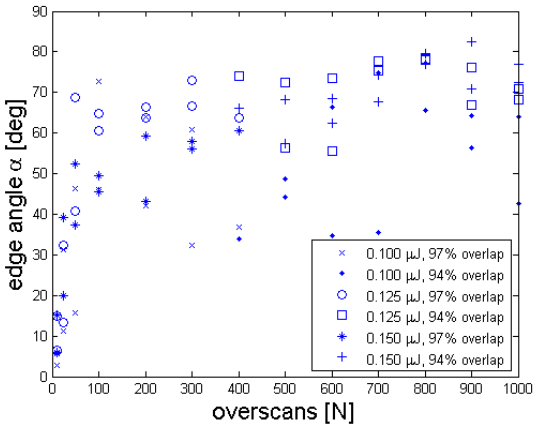

Fig. 17 Measured edge angle as a function of pulse energy, overlap and number of overscans at 400 kHz.

It can be observed from Figure 16 and 17 that, for a fixed pulse energy, the edge angle increases significantly, from about 10° to about 65°, when increasing overscans from N=10 to 100. At higher number of overscans, so N>100, the edge angle gradually increase towards 90°. However, for pulse energies near or below the ablation energy, so E_p≤0.1µJ, the edge angle shows an irregular trend as a function of overscans N.

From these results, processing conditions were selected to create trenches with the targeted depths, see Table 1.

Table 1 Processing conditions to create trenches.

Parameter set	Targeted depth [µm]	E_p [µJ]	Over-Lap [µm]	N [#]	f_p [Hz]
1	0.5	0.1	1	25	400
2	1	0.125	1	50	400
3	2	0.225	0.5	10	50
4	5	0.225	0.5	50	50

These sets of parameters were chosen, from Figure 12 and 13, such that the track edge depth d_e was close to the targeted depth. For parameter set 4 (Table 1) the process parameters were chosen such that the track center depth d_c was near the intended depth of 5.0µm, as the track edge depth has an upper limit of about 2.5µm. If, in any case there were multiple candidates, a parameter set, that yields the sharpest edge angles, was chosen. Table 2 lists the measured depth and edge angle of the ablated lines per parameter set, as measured by CLSM. The extreme values are listed, with the average values between brackets.

Table 2 Measured geometrical properties of the tracks.

Param. set	Depth [µm]	α [deg]
1	0.362 - 0.778 (0.546)	13.6 – 37.9 (26.4)
2	0.542 - 2.310 (1.311)	20.1 – 83.8 (38.1)
3	1.665 – 2.519 (2.023)	9.9 – 29.3 (19.3)
4	5.359 – 11.1667 (8.408)	42.5 – 52.4 (45.8)

As can be concluded from this data, the depth and edge angle show some spread. This can be attributed to the initial surface roughness of the leadframe. The targeted depths of the trenches are in the same order of magnitude as the roughness of the unmachined leadframe. Laser ablation to a depth of less that this roughness will result in a irregular edge depth and edge angle.

4.3 Processing conditions for trenches for receptor sites

To create trenches wider than the width of a single ablated track, several parallel laser tracks were machined next to each other, to create an "area" of ablated material. Striving for a flat bottom of the trench, the hatch distance was chosen to be about one third of the width of a single laser track. Hence, 2µm, 1.9µm, 4.3µm and 4.8µm, for parameter set 1 to 4 respectively. Targeted trench width is about 100µm, to ensure that the droplet used for self-alignment experiments will not be affected by the width of the trench. Next, every area was rescanned N times (overscans). By creating four of these areas in a square pattern, square receptor sites were obtained, see Figure 18. Note that, the horizontal and vertical trenches overlap in the corners resulting in 2N overscans at those locations.

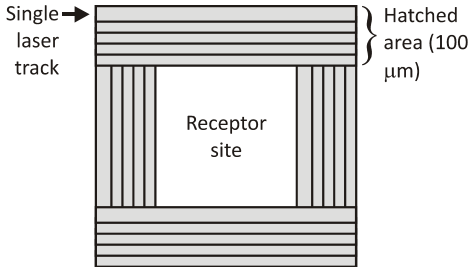

Fig. 18 Four hatched areas, in a square pattern, consisting of overlapping laser tracks each, yield a square receptor site.

As a result of these double overscans the depth of the trench at the corners will be larger than the depth along the side of the site, see Figure 19. These corner areas will not have a negative effect on the liquid confinement capability of the site.

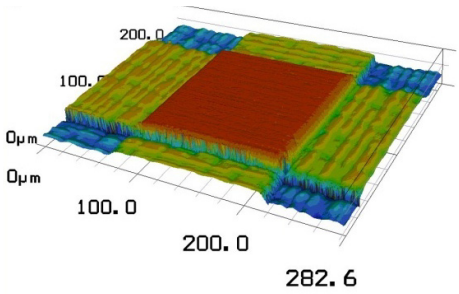

Fig. 19 CLSM image of a receptor site with sharp edges, created with processing conditions of parameter set 4.

4.4 Liquid confinement experiments

Liquid confinement experiments have been performed on the 5×5 mm^2 receptor sites, using the OCA15plus, to determine to determine the dependence of the confinement on the edge angle α. Figure 20 shows a typical droplet of water, released from a needle and confined by a receptor site. Figure 21 shows the volume of liquid pinned by the receptor site as a function of the edge angle α.

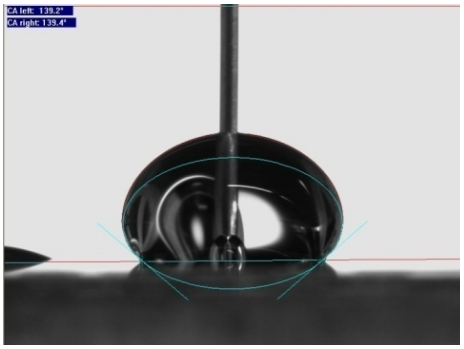

Fig. 20 Liquid confinement test and static contact angle measurement (using the using the OCA15plus set-up) on a receptor site created using parameter set 4.

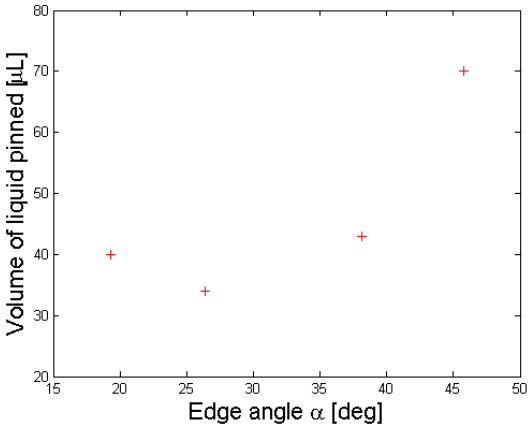

Fig. 21 Liquid confinement ability of the edges on 5x5 mm^2 receptor areas.

The figure shows that, the volume of liquid that is pinned on the 5×5mm^2 receptor site increases with increasing edge angle α. The liquid confinement ability of the small, 210×210µm^2, receptor sites was tested, using the robotic microassembly setup, by continuously dispensing small droplets on the receptor areas until a single large droplet was formed. Pictures were taken from the side, just before the large droplet started spreading over the edges of the receptor site. Volumes of the confined droplets were estimated by assuming the droplets have the shape of a spherical cap, which is a valid assumption when the scale under study is well below the capillary length. Confined droplets on sites with different edge angles α are shown in Figure 22 and their relationship is shown in Figure 23. The results show that the maximum volume of confined water droplet increases with increasing edge angle.

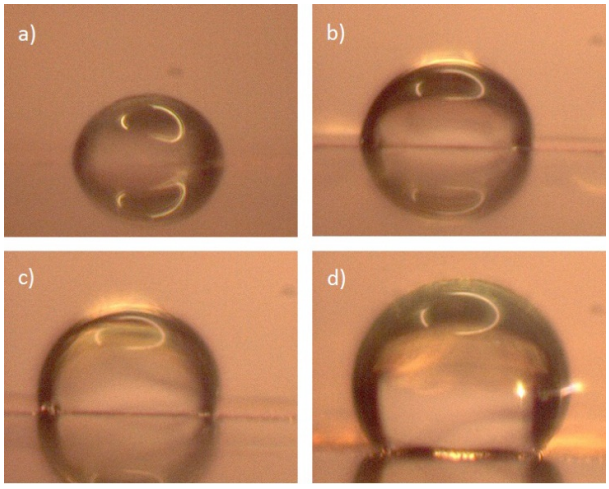

Fig. 22 Water droplet confinement on receptor sites.
(a) Parameter set 1, contact angle: 68°, volume: 1.4 nl,
(b) Parameter set 2, contact angle: 90°, volume: 2.4 nl,
(c) Parameter set 3, contact angle: 102°, volume: 3.4 nl,
(d) Parameter set 4, contact angle: 127°, volume: 8.5 nl.

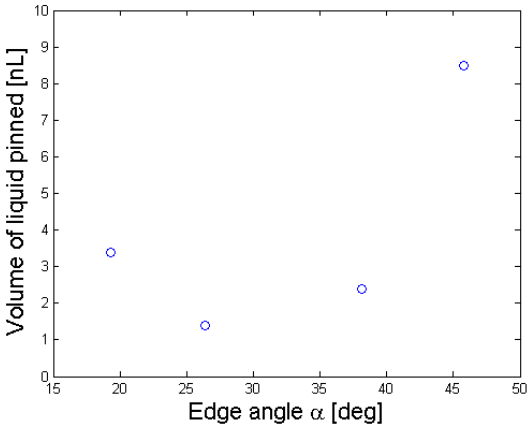

Fig.23 Liquid confinement capability of the receptor sites with dimensions 210×210 μm^2.

4.5 Self-alignment experiments

Self-alignment tests, using the set-up described in section 3.4, were performed on laser patterns with different heights. Dimensions of the sites were 200×200μm^2 and 110×110μm^2. And 50μm thick SU-8 chips with corresponding sizes were used as parts to be aligned. The experiment comprised of the following steps:

1. the chip is moved to a predefined releasing position near the receptor site,
2. a droplet of water is dispensed on the site and the chip is released on it,
3. then the chip is self-aligned to the site,
4. in a few seconds, water vaporizes, leaving the chip on the receptor site.

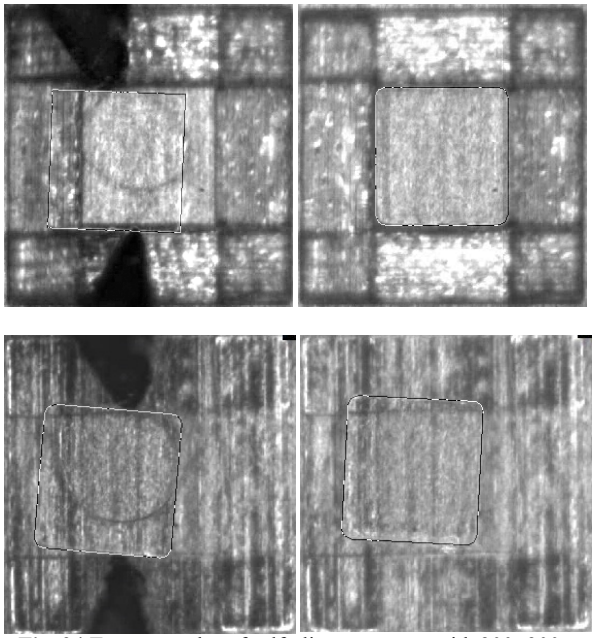

Fig. 24 Two examples of self-alignment tests with 200×200μm SU-8 chips, where the edges of the chip have been highlighted. Top row: chip at releasing position (left) and final position after successful self-alignment (right). Bottom row: chip at releasing position and final position after failed self-alignment.

Figure 24 shows two examples of the self-alignment tests, where the top one is a successful case and the bottom one shows a failure case. The results of initial self-alignment tests are summarized in Table 3. Here, success rates are presented for each pattern height and site size combination. For each pattern height the tests were repeated six times for 200×200μm^2 patterns and three times for 110×110μm^2 patterns. The volume of water droplets were estimated as 0.22nl for 200×200μm^2 sites and 0.05nl for 110×110μm^2 sites, based on the captured video image. The results suggest that the height of the patterns is critical for self-alignment, which became more reliable with increasing height. However, it should be noted that the initial surface roughness of 1.5μm will most probably have a strong effect for the success rate of site height of 0.5 to 2μm. For pattern height of 5μm, self-alignment succeeded in all the tests. Self-alignment on smaller patterns (110×110μm^2) seems to be difficult. Further tests are required to understand the influence of pattern size on self-alignment.

Table 3 Success rates of self-alignment on receptor sites.

Pattern size/pattern height [μm]	200×200 [μm^2]	110×110 [μm^2]
0.5	0%	0%
1	33%	0%
2	66%	0%
5	100%	100%

5. Conclusions and future work

A ps laser, operating at 343nm wavelength, 50kHz and 400kHz, with a focus diameter of 15.6μm was used to create receptor sites with areas ranging from 110×110μm^2 up to 5×5mm^2, and heights ranging from 0.5μm to 5μm. Spreading of liquid from these sites were shown to be stopped by a sharp geometrical edge around the site. That is, it was found, by video based optical contact angle measurement, that the volume of water that is pinned on the receptor site increases with increasing angle of the edges of the receptor site. In addition, it was found, by using a robotic microassembly system, that the success rates of self-alignment of 110×110μm^2 parts, as well as 200×200μm^2 parts, on the receptor sites is 100% if the angle of the edges of the receptor site are sharp, and the height of the receptor site is well over the initial surface roughness of the substrate.

Future work will include beam shaping to obtain a steep power density profile, e.g. a square uniform profile or a tophat profile, instead of the Gaussian profile. It is expected that machining with these steeper profiles will result in receptor sites with edge angles approaching 90°. In addition, laser machining methods to create edge angles over 90° will be studied.

The transparent chips used in self-alignment tests usually brings better understanding of the assembly process, but it appears difficult to identify details with the complex background surface of the receptor site. Fabricated silicon chips will be used in future tests to provide more identifiable results.

Acknowledgments

The authors would like to acknowledge the financial support of the European Union Seventh Framework Programme FP7-2010-NMP-ICT-FoF under Grant Agreement **N**°. 260079 - *Efficient and Precise 3D Integration of Heterogeneous Microsystems from Fabrication to Assembly***.** http://www.fab2asm.eu.

References

[1] D. Arnaldo del Cerro, G.R.B.E. Römer, A.J. Huis in 't Veld, Picosecond laser machined designed patterns with anti-ice effect, Proceedings of the 11th International Symposium on Laser Precision Microfabrication, (2010).

[2] G.R.B.E. Römer, G.R.B.E., A.J. Huis in 't Veld, J. Meijer, M.N.W. Groenendijk, On the formation of laser induced self-organizing nanostructures. CIRP Annals, 58 (1). pp. 201-204. (2009).

[3] K.F. Böhringer, U. Srinivasan, R.T. Howe, Modeling of capillary forces and binding sites for fluidic self-assembly, Proceedings of the International Conference on Micro Electro Mechanical Systems (MEMS'01), pp. 369-374, (2001).

[4] V. Sariola, M. Jääskeläinen, Q. Zhou, Hybrid Microassembly Combining Robotics and Water Droplet Self-Alignment, IEEE Transactions on Robotics, 26(6), pp. 965 – 977, (2010).

[5] S.H. Liang, X. Xiong, K.F. Böhringer, Towards optimal designs for self-alignment in surface tension driven micro-assembly, Proceedings of the 17th IEEE International Conference on. (MEMS) Micro Electro Mechanical Systems, pp. 9-12, (2004).

[6] V. Sariola, Q. Zhou, H.N. Koivo, Three dimensional hybrid microassembly combining robotic microhandling and self-assembly, 2009 IEEE International Conference on Robotics and Automation, (2009).

[7] V. Sariola, Q. Zhou, R. Laass, H.N. Koivo, Experimental study on droplet based hybrid microhandling using high speed camera, 2008 IEEE/RSJ Internaional Converence on Intelligent Robots and Systems, (2008).

[8] A. Tuteja, W. Choi, M. Ma,J.M. Mabry, S.A. Mazzella, G.C. Rutledge, G.H. McKinley, R.E. Cohen. Designing Superoleophobic Surfaces. Science **318**, 1618 (2007)

[9] P-G. de Gennes, F. Brochard-Wyart, D. Quere, Capillarity and Wetting Phenomena: Drops, Bubbles, Pearls, Waves. Springer. Springer, 2004.

[10] X.M. Li, D. Reinhoudt, M. Crego-Calama, What do we need for a superhydrophobic surface? a review on the recent progress in the preparation of superhydrophobic surfaces, Chemical Society Reviews 36 (8) (2007) 1350–1368.

[11] T. Young, An essay on the cohesion of fluids, Philosophical Transactions of the Royal Society of London 95 (1805) 65–87.

[12] N. A. Patankar, On the modeling of hydrophobic contact angles on rough surfaces, Langmuir 19 (4) (2003) 1249–1253.

[13] H. Y. Erbil, A. L. Demirel, Y. Avci, O. Mert, Transformation of a simple plastic into a superhydrophobic surface, Science 299 (5611) (2003) 1377–1380.

[14] R.N. Wenzel, Resistance of solid surfaces to wetting by water, Industrial and Engineering Chemistry 28 (8) (1936)988–994.

[15] A. B. D. Cassie, S. Baxter, Wettability of porous surfaces, Transactions of the Faraday Society 40 (1944) 546–551.

[16] A. Nakajima, K. Hashimoto, T. Watanabe, Recent studies on super-hydrophobic films, Monatshefte f¨ur Chemie /Chemical Monthly 132 (1) (2001) 31–41.

[17] J.W. Gibbs. Scientific Papers Vol. 1, Longmans, London (1906), p. 326 (Dover reprint, New York, 1961).

[18] J. F. Oliver, C. Huh, S. G. Mason, Resistance to spreading of liquids by sharp edges, Journal of Colloid and Interface Science 59 (3) (1977) 568–581.

[19] A. M. Kietzig, S. G. Hatzikiriakos, P. Englezos, Patterned superhydrophobic metallic surfaces, Langmuir 25 (8) (2009) 4821–4827.

[20] V. Zorba, E. Stratakis, M. Barberoglou, E. Spanakis, P. Tzanetakis, C. Fotakis, Tailoring the wetting response of silicon surfaces via fs laser structuring, Applied Physics A: Materials Science amp; Processing 93 (4) (2008) 819–825.

[21] G.R.B.E. Römer and A.J. Huis in 't Veld. Matlab Laser Toolbox. In: Laser Assisted Net Shape Engineering 6, Proceedings of the LANE 2010. Physics Procedia, 5 (Part 2). Elsevier, pp. 413-419 (2010)

[22] J. Bonse, J.M. Wrobel, J. Kr¨uger, and W. Kautek. Ultrashort-pulse laser ablation of indium phosphide in air. Applied Physics A, 72(1):89–94, 2001.

[23] J. Bonse, S. Baudach, J. Krüger, W. Kautek, and M. Kenzner. Femtosecond laser ablation of siliconmodification thresholds and morphology. Applied Physics A, 74(1):19–25, 2002.

[24] Y. Jee, M.F. Becker, and R.M. Walser. Laser-induced damage on single-crystal metal surfaces. Journal of the Optical Society of America B., 5(3):648–658, 1988.